Protection scheme for multi-terminal HVDC system with superconducting cables based on artificial intelligence algorithms

Eleni Tsotsopoulou [a,*], Xenofon Karagiannis [b], Theofilos Papadopoulos [b], Andreas Chrysochos [c], Adam Dyśko [a], Dimitrios Tzelepis [a]

[a] Department of Electronic and Electrical Engineering, University of Strathclyde, Glasgow, G1 1XQ, UK
[b] Department of Electrical and Computer Engineering, Democritus University of Thrace, Xanthi, Greece
[c] R&D Department of Hellenic Cables, Athens, 15125, Greece

ARTICLE INFO

ABSTRACT

This paper presents the development of a novel data-driven fault detection and classification scheme for DC faults in multi-terminal HVDC transmission system which incorporates superconducting cables and modular multi-level converters. As the deployment of superconducting cables for bulk power transmission from remote renewable generation is progressively increasing in the future energy grids, many fault-related challenges have been raised (i.e., fault detection, protection sensitivity/stability). In this context, the applications of Artificial Intelligence techniques have started to be considered as a powerful tool for the development of robust fault management solutions. The proposed artificial intelligence-based method utilizes local current and voltage measurements to detect and classify all types of faults on the DC cables and DC buses, without the requirement of measurements exchange among different DC substations. The performance of the proposed scheme has been assessed through detailed transient simulation analysis and the results confirmed its effectiveness against a wide range of fault conditions (i.e., various fault types, fault locations and fault resistances). Furthermore, the feasibility of the developed scheme for real-time implementation has been validated using real-time software in the loop testing. The results revealed that the proposed algorithm can correctly, and within a very short period of time (i.e. less than 2 ms) detect and classify the faults within the protected zone and concurrently remain stable during external faults. Additionally, the generalization capability of the algorithm has been verified against influencing factors such as the addition of noise, highlighting the robustness of the presented scheme.

1. Introduction

The accelerated uptake of Renewable Energy Source (RES)-based technologies (i.e, wind farms (WFs) and PV systems) coupled with the continuous and rapid growth of the global electricity demand and the ageing of the existing system's infrastructure have a great impact on the power system operation and resiliency. Therefore, the development of bulk power corridors for connecting RES and providing electric power sharing over long distances, is rendered imperative to address the congestion challenges and ensure the security of supply. On that front, the Modular Multilevel Converter (MMC)-based High-Voltage Direct Current (HVDC) transmission technology has started to receive increasing attention in the energy sector [1].

Multi-terminal HVDC systems, as a natural extension of the existing point-to-point HVDC grids, satisfy all the requirements for enabling the target of energy connectivity without borders. However, a key challenge for the realization of meshed HVDC systems is the detection and clearance of the DC-side faults due to the rapid rise of the DC fault currents and the absence of natural current zero-crossing [2,3]. In this context, the fault clearance process of the DC-side faults requires very fast and discriminative protection schemes which detect and isolate the fault within the range of 5 ms [4,5]. Furthermore, as the transient performance of the Superconducting Cables (SCs) is dominated by the quenching phenomenon and the electro-thermal properties of the High Temperature Superconducting (HTS) tapes [6], their installation within the meshed HVDC systems introduces new variables to the system's operation (i.e., variable impedance, reduced fault current magnitudes etc.) and leads to many fault management challenges, accounting for the fault detection/isolation and protection sensitivity/stability. Therefore, it is realized that for the secure and reliable operation of the meshed HVDC grids with DC SCs the development of advanced protection solutions complied with the DC protection requirements, is vital.

During the last few years, as the technology of superconducting applications progresses, many initiatives exploited the unique features of the DC SCs (i.e., high efficiency, low losses and compact size [7]) and promoted the deployment of such cables in HVDC grids for the bulk power transfer (notably from offshore WFs) [8]. The first DC SC for industrial application was accomplished by the Chinese Academy of Science in 2012 by designing a 1.3 kV/10 kA unipolar cable with length 360 m [9]. To date, there are three landmark demonstration projects of DC SCs. In particular, the EU-funded Best Paths project, which investigates and validates the operation of a 30 m, 320 kV/3.2 GW HVDC link for real-grid conditions with the developed technology to approach the commercial deployment [10]. The Ishikari project, Japan, which demonstrates the deployment of 500 m and 1000 m DC SCs for the interconnection between a large scale PV cell with an Internet data center to provide DC power supply [11] and the St. Petersburg project which deploys the installation of a 2.5 km length DC SC at 20 kV operating temperature [12]. Furthermore, many researchers have started to investigate the technical feasibility and the associated challenges of the meshed HVDC grids with SCs. Specifically, authors in [13] addressed the power flow and transient stability issues of multi-terminal HVDC systems with Voltage Source Converters (VSCs) and SCs, while a feedback current control scheme to regulate the power distribution in a meshed HVDC systems with SCs and Line Commutated Converters (LCCs) was developed in [14]. A detailed fault current characterization of meshed HVDC system with MMCs and DC SCs is presented in [15]. The conducted simulation-based analysis evaluated the impact of the SC fault current limiting capability on the DC fault current magnitudes, highlighting the potential of higher flexibility in terms of protection operation time. All the existing studies carried out series of tests on prototype SCs or simulations-based analysis in order to assess the steady-state/transient performance and the mechanical suitability of the DC SCs or to validate the cable design process and the operation of the cryogenic refrigeration system. However, there is no reported research, discussions or proposed strategies for the fault management of DC SCs (i.e., fault detection, location, protection coordination), presenting barriers to the widespread adoption of such cable technology in large-scale HVDC applications.

Driven by this research gap, this paper proposes a novel data-driven centralized protection scheme (on the substation level) for discriminative fault detection and isolation in multi-terminal HVDC systems with DC SCs and conventional DC cables. The developed protection strategy exploits the potential of the latest advancements in Artificial Intelligence (AI) classifiers, is suitable for HVDC substation, and presents the capability of classifying/detecting faults occurring to all the elements collected to it (i.e., buses, SCs and conventional feeders).

The principal contribution of the presented work is laid out thereafter:

- Detailed fault analysis assessment of DC SCs to reveal the protection challenges caused by their deployment in meshed HVDC systems.
- Evaluation of existing HVDC protection scheme performance for the adequate fault detection on SCs in meshed HVDC systems.
- Development of a novel data-driven protection scheme, for rapid and discriminative fault detection and classification in meshed HVDC system with SCs. The proposed scheme adopts centralized protection philosophy (on the substation level) and is designed to detect and classify faults in HVDC substations accounting for bus faults and faults applied on SCs or conventional feeders. The proposed algorithm is considered a suitable solution for meshed HVDC systems with SCs as it presents robust performance under the influence of different fault conditions and stability against noisy measurements. Furthermore, it is applicable for real-time implementation as its performance has been validated through real-time Software-In-the-Loop (SIL) testing.

Table 1
System specifications.

Parameter	Symbol	Value
AC onshore voltage	V_{ACON}	400 kV
AC offshore voltage	V_{ACOF}	66 kV
Rated current of CC and SC1	I_{rated}	2 kA
Rated current of SC2	I_{rated}	2.2 kA
DC voltage	V_{DC}	200 kV
DC inductor for SC1	L_{DC}	140 mH
DC inductor for SC2	L_{DC}	145 mH
MMC arm inductor	L_{arm}	0.1 p.u.
Cells per arm	C_{SM}	400
Conventional cable resistance	R_{Cable}	0.0146 Ω/km
Conventional cable inductance	L_{Cable}	0.158 mH/km
Conventional cable capacitance	C_{Cable}	0.275 μF/km

2. Topology of multi-terminal HVDC system with DC SCs and conventional cable

2.1. System under test

Fig. 1 presents the overall topology of the three-terminal HVDC grid model developed in Matlab/Simulink. The system architecture is based on the concept proposed in [3] and considers the power transmission from a 66 kV AC offshore WF to 400 kV onshore AC grid, through DC SCs. The system is developed by adopting a symmetric monopole configuration and consists of three MMCs operating at ±200 kV and current-limiting inductors connected at each cable end.

MMC3 operates in grid-forming control mode for the integration of the power delivered by the WF. MMC1 is utilized for the DC voltage control of the HVDC meshed network, while the MMC2 controls the active P and reactive Q power exchange with the onshore AC grid 1. Specifically, 0.4 GW of offshore power is transmitted to onshore AC grid 1. Two bipolar DC SCs have been integrated within the system to connect the Bus 3 with Bus 1 and Bus 2, respectively. The length of SC1 and SC2 is 100 km and 120 km, respectively and are utilized for the bulk offshore power transmission with approximately zero losses. For the fabrication of such long DC SCs, joints are utilized to connect HTS tapes and provide electrical continuity [15–17]. The electro-thermal modelling process of the SCs will be analysed in Section 2.2. It is worthy of note that the detailed modelling of SC joints is beyond the scope of the presented work.

Bus 1 and Bus 2 are connected through a DC Conventional Cable (CC) developed according to the distributed parameters model [18]. All cables sheaths are solidly bonded. The specifications of the AC and DC side of the system are demonstrated in Table 1.

2.2. Modelling of DC SCs

This section presents the mathematical formulation of coupled electro-thermal modelling of the coaxial DC SC illustrated in Fig. 2. The configuration of the developed cable consists of two concentric poles, the positive and negative pole [19]. The current passing through the negative pole is nearly identical to the current flowing through the positive pole, but with opposite direction. Each pole is composed of one layer of HTS tapes, which have been modelled as coated conductors, and a copper stabilizer layer which is utilized as an alternative current path during quenching to provide electrical and thermal support to HTS layers. The structure of the employed HTS tapes has been based on the specifications proposed by SuperPower [20] and the detailed modelling has been presented in [21]. The detailed modelling of HTS tapes has been presented by authors in the work conducted in [21]. The number of HTS tapes has been selected considering the derating factor, given by (1), which expresses the ratio between the operating current at superconducting state, I_{op}, and the critical current, I_C, of HTS tapes [22–24]:
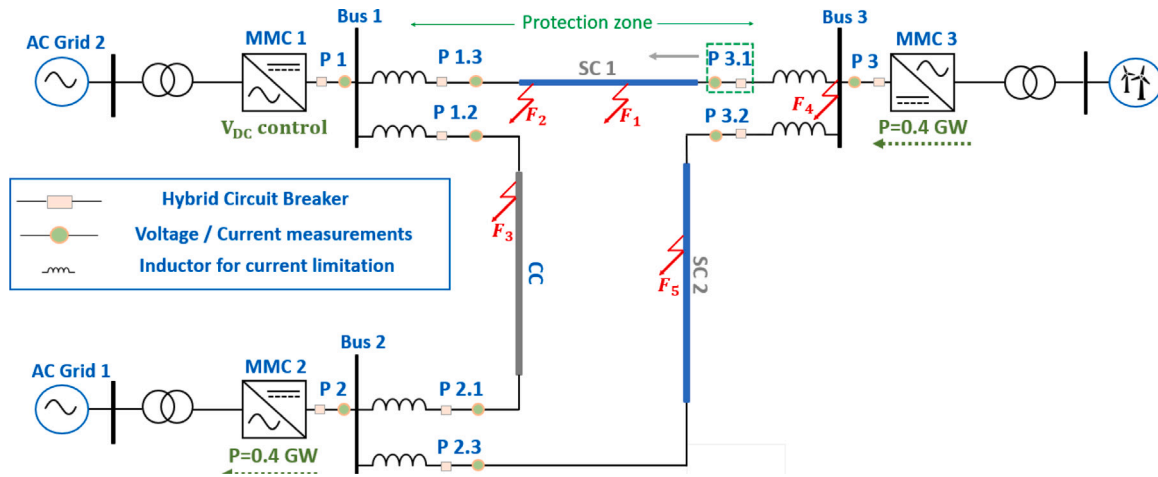
$$derating\ factor = \frac{I_{op}}{I_C} = 80\% \tag{1}$$
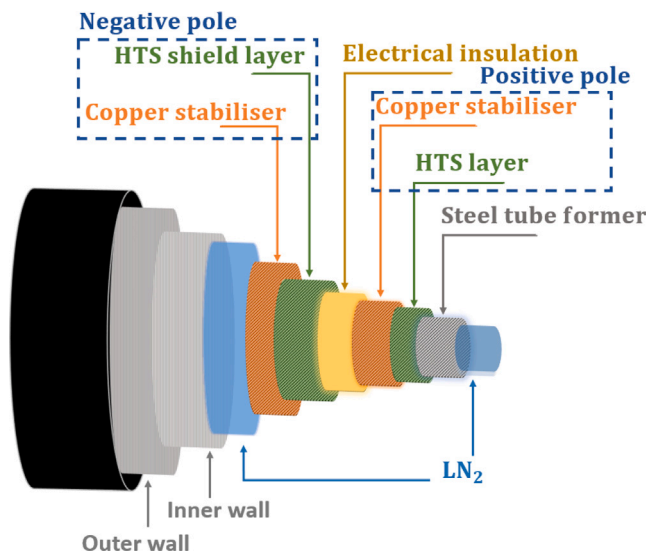
Fig. 1. HVDC network model incorporating SCs and CC.

Fig. 2. Schematic illustration of coaxial DC SC.

Table 2
Parameters of HTS tape and geometrical characteristics of SC.

Parameter	Symbol	Value
Tape width	w_t	4 mm
Tape length of SC1/SC2	l_t	100/120 km
Tape critical current of SC1/SC2	I_C	140/120 A
Tape critical temperature	T_C	92 K
Thickness of YBCO	t_{YBCO}	1 μm
Thickness of copper stabilizer	th_{Cu}	40 μm
Thickness of substrate	th_{sub}	60 μm
Radius of HTS conducting layer and copper of SC1/SC2	$r_{HTS_c+copper}$	15.14/17.50 mm
Radius of electric insulation of SC1/SC2	r_{ins}	27.14/29.50 mm
Radius of HTS shield layer and copper of SC1/SC2	$r_{HTS_s+copper}$	27.28/29.64 mm
Radius of outer wall of SC1/SC2	r_{out}	110.23/111.34 mm
Density of YBCO	d_{YBCO}	5900 kg/m³
Density of stainless steel	d_{steel}	7500 kg/m³
Density of copper	d_{Cu}	8940 kg/m³
Density of PPLP	d_{PPLP}	0.9 kg/m³
Specific heat of Cu	c_{Cu}	185 J/kg K
Specific heat of Steel	c_{psteel}	185 J/kg K
Specific heat of PPLP	c_{pPPLP}	1930 J/kg K

The Yttrium Barium Copper Oxide (YBCO) second generation (2*G*) superconducting material has been adopted for the modelling of HTS tapes. An electrical insulation layer, made of Polypropylene Laminated Paper (PPLP), is placed between the positive and negative poles. The thickness of dielectric material has been chosen in accordance with the voltage level of DC grid. For the cooling of the DC SC, liquid nitrogen (LN_2) has been selected as a coolant to sustain a constant temperature within the range of 65–70 K. All layers are contained within a cryostat which provides thermal insulation. For simplification of the electromagnetic performance of SC, the current distribution between HTS tapes and the current density, J, distribution among each tape have been considered uniform [22]. The parameters of HTS tape and the geometrical characteristic of the developed SCs are summarized in Table 2.

The superconducting state of SCs is defined by three interdependent critical boundaries accounting for the critical temperature, T_C, critical current density, J_C, and critical magnetic field, H_C. The critical margins are dependent on the design of SC and the system operating conditions. HTS tapes and consequently SC, lose their superconducting properties and transit to non-superconducting state, known as normal highly-resistive state, if any of the critical boundaries is exceeded. The transition from superconducting state to normal highly resistive state

can be described by the $E − J$ power law and the resistivity, ρ_{YBCO}, of the superconducting material is given by (2):

$$\rho_{YBCO} = \frac{E_C}{J_C(T)} \cdot \left(\frac{J}{J_C(T)} \right)^{n-1} \tag{2}$$

where $E_C = 1$ μV/cm refers to the critical electric field, J denotes the operating current density, n is a factor which defines the sharpness of the transition to highly resistive state, J_C is the critical current density and is calculated as a function of the temperature, T, according to [15,25].

When SC operates at superconducting state, J is below J_C, T is below T_C and $\rho_{YBCO} = 0$. During transient conditions, when the current flowing through SC increases, J exceeds the value of J_C, leading to the quenching initiation. Under these conditions, ρ_{YBCO} presents a non-linear increase according to (2) and SC enters to flux-flow state. The rapid increase in ρ_{YBCO} and accordingly in resistance of YBCO layer, R_{YBCO}, of HTS tapes leads to heat generation and consequently results in the rise of SC T. Once T of SC surpasses the value of T_C, SC reaches the normal highly resistive state and the operating current is redistributed towards the copper stabilizer layers and former which present lower resistance. The resistivity, ρ_{Cu}, of copper stabilizer layers and ρ_{steel} of former are given as functions of T by (3) and (4), respectively [15]:

$$\rho_{Cu} = (0.0084 \cdot T - 0.4603) \cdot 10^{-8}, \quad 250 \text{ K} > T \geq 70 \text{ K} \tag{3}$$

$$\rho_{steel} = 1.193 \cdot 10^{-6} - 7.529 \cdot 10^{-7} \exp(-T/647.113) \tag{4}$$

The equivalent resistance of SC, R_{eq}, changes with respect to the operating state of HTS tapes. At superconducting state, SC presents perfect conductivity and R_{eq} is approximately zero. Once quenching is triggered, the current is shared among the HTS layer, copper stabilizer layers and former which have been modelled as parallel resistors. In the presented work, for modelling purposes R_{eq} of SC has been considered as the equivalent resistance of the parallel connected R_{YBCO}, R_{Cu} and R_{former}, respectively [15,21]. The value of R_{eq} has been calculated as piecewise function of T similarly to [15,25].

Considering the electro-thermal coupled modelling of SC, the sudden loss of the superconducting behaviour during quenching is translated into Joule heat generation by the superconductor. Assuming that there is no heat transfer with the external environment, part of the generated Joule heat leads to the increase of T and the rest is absorbed by the LN_2 cooling system. By adopting the law of conservation of energy, the net power of the SC is calculated by (5):

$$P(t)_{SC} = P(t)_{diss} - P(t)_{cooling} \tag{5}$$

where $P(t)_{diss}$ is the Joule heating generated by the SC, due to the variations in R_{eq} during quenching, and $P(t)_{cooling}$ is the cooling power removed by LN_2 refrigeration system. The analytical equations of $P(t)_{diss}$ and $P(t)_{cooling}$ are given in [15,26].

Eventually, the increase in T of SC can be calculated through (6):

$$T(t) = T_{t-1} + \frac{1}{C_{pSC}} \cdot \int_0^t P(t)_{SC} \, dt \tag{6}$$

where C_{pSC} J/K denotes the total heat capacity of the superconductor and is calculated as a function of the specific heat and mass ($density \cdot Volume$) of the material of each SC layer. The specific heat and density of each material are given in Table 2.

Furthermore, the presented modelling approach considers the magnetic coupling caused by the geometry of SC. The final values of the capacitance, C, and inductance, L, (per-unit length values) of SC1 and SC2 have been calculated utilizing the general formulation proposed in [27] and considering frequency of 10^{-3} Hz [4]. In particular, the final values are obtained based on the full 4×4 impedance and admittance matrices which consider the mutual coupling between the HTS shield and HTS conducting layers.

The electro-thermal characteristics of the SCs have been modelled in Matlab/Simulink following the procedure proposed by some of the authors in [25]. Specifically, the electro-thermal modelling of the SCs can be formulated by combining (2) to (6) based on which the flowing current through the SC is translated into Joule heat generation and consequently the temperature variations are translated into the changes in the resistivity of the different layers. During the simulation process, the temperature, the resistance of each layer and the current distribution among the layers are calculated in each simulation time step.

3. Fault characterization of SCs

Prior to the development of the proposed protection scheme, the characterization of the SCs behaviour during transient conditions is of paramount importance. The fault analysis of SCs plays a vital role in preserving power system safety and reliability. Therefore, the ultimate goal of this section is to acquire a deeper understanding of DC SCs quenching and consequently to quantify the challenges from power systems protection perspective.

For this purpose a series of different fault scenarios have been investigated by conducting Electro-Magnetic Transient (EMT) simulation studies and utilizing the system depicted in Fig. 1. The fault scenarios include Pole-to-Pole (PP), positive Pole-to-Ground (PG) and negative Pole-to-Ground (NG) faults (incorporating various fault positions along the SCs and CC and different values of fault resistance) and faults applied at buses. The simulation results of four representative fault

Table 3
Representative fault scenarios.

Scenario	Fault type	Fault location	Fault resistance
F_1	PP	20% of SC1 length (internal)	0 Ω
F_2	PP	99% of SC1 length (internal)	300 Ω
F_3	PP	0.1% of CC length (external)	0 Ω
F_4	PP	Bus 3 (external)	0 Ω

scenarios are presented in the following subsections. The selected scenarios aim to analyse the performance of SCs during the quenching phenomenon, the impact of the fault resistance on the quenching process and the effect of external faults, applied at CC and buses, which lead to quenching of the SCs. Table 3 summarizes the presented fault scenarios which include a PP internal solid fault applied at SC1 ($F1$), a PP highly-resistive internal fault applied at remote end of SC1 ($F2$), a PP external solid fault at CC ($F3$) and a PP external solid fault occurring at Bus 3 ($F4$). During all the scenarios the faults have been applied at $t = 5$ ms and are permanent. Furthermore, it should be noted that for each scenario R_{eq} of each SC and the total current flowing through SC are presented, as they are key factors which affect the fault detection and classification process. The investigation of the resistance change along with current variations in each layers of SC is beyond the scope of the presented work.

3.1. Scenario F_1

Fig. 3 demonstrates the response of SC1, SC2 and CC under the influence of a PP solid fault applied at 20% of the SC1 length (i.e., 20 km from Bus 3). Fig. 3a shows the DC currents flowing through the SC1, SC2 and CC. During steady state conditions, the current flowing through SC2 is approximately 2 kA, while the current flowing through SC1 and CC is approximately 0 A. These simulation results show that during normal operation the offshore wind power (0.4 GW) is transmitted to onshore AC grid 1 (depicted in Fig. 1) through SC2. The fault occurred at $t = 5$ ms, 0.15 ms after the fault occurrence, SC1, which is the faulted one, starts to quench and the peak of the fault current is 8.96 kA. During the quenching process, R_{eq} of SC1 increases, (i.e., refer to Fig. 3c), and the maximum value reached is approximately 120 Ω. The rapid increase in R_{eq} leads to generation of Joule heat and consequently causes an abrupt increase in T of SC1 (Fig. 3d). The SC1 operates at highly-resistive state, causing a reduction to the DC fault current which is sustained to approximately 7 kA. The pole-to-pole voltage of SC1 is depicted in Fig. 3b, and is depressed to 30 kV, when quenching is initiated, and increases up to 60 kV with the reduction of the DC fault current. The current infeed from SC2 and CC are demonstrated in Fig. 3a and the rate of current rise is limited due to the inductive terminations. It should be noted that the solid fault applied on SC1 does not cause the quenching of SC2 and consequently T and R_{eq} of SC2 are sustained to 70 K (Fig. 3d) and 0 Ω (Fig. 3c), respectively.

Considering the results from this scenario, it is evident that the proper design of the HTS tapes can provide fault current limiting functionality to the SCs which leads to the suppression of the fault current during the fault period. Therefore, the deployment of DC SCs in HVDC systems leads to the reduction of the fault current magnitudes, eliminating the stress across the CBs.

3.2. Scenario F_2

Fig. 4 presents the transient performance of SC1, SC2 and CC during a highly-resistive (fault resistance, $R_f = 300$ Ω,) PP, fault applied at 99% of the SC1 length (99 km from Bus 3). Fig. 4a shows the DC fault currents of SC1, SC2 and CC. It is evident that SC1 does not quench during this fault scenario as the fault current flowing through HTS tapes is predominantly limited by R_f and therefore does not exceed the
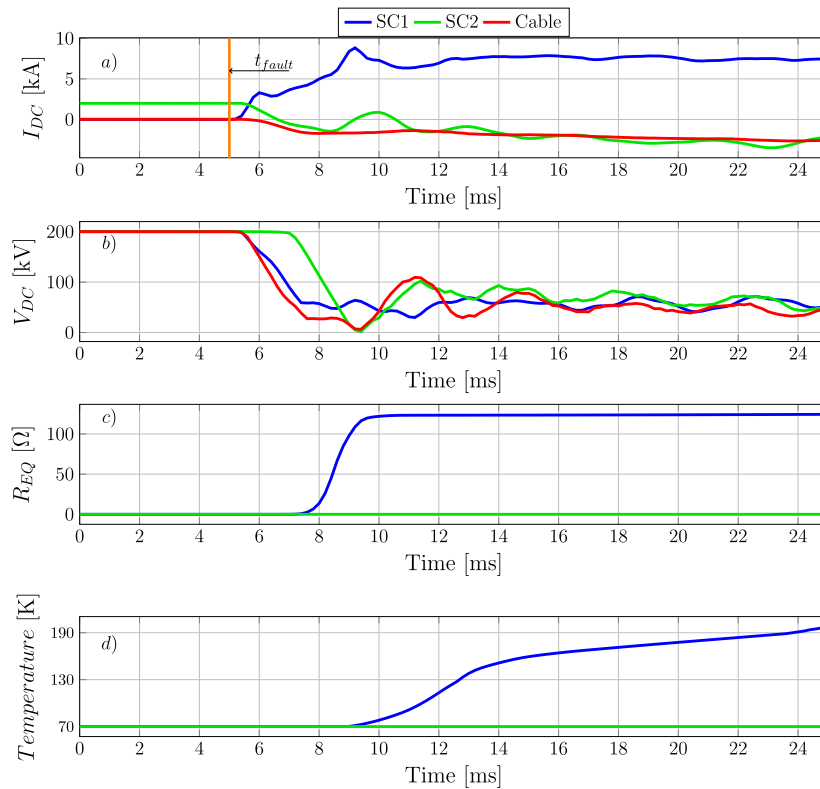
Fig. 3. PP solid fault at 20% of SC1 length: (a) SC1, SC2 and CC DC currents, (b) SC1, SC2 and CC DC pole-to-pole voltage, (c) equivalent resistance of SC1 and SC2, (d) temperature of SC1 and SC2.

value of I_C. Specifically, during normal conditions the current flowing though SC1 is approximately 0 A, as the offshore power is transmitted to onshore AC grid 1 through SC2. Once the fault occurred, the peak current of SC1 is approximately 250 A, the voltage is slightly reduced to 198 kV (Fig. 4b) and as observed in Fig. 4c and d, SC1 continues to operate at superconducting state with R_{eq} being 0 Ω and T 70 K.

Furthermore, SC2 maintains the superconducting properties during the fault period, operating as a zero resistance path (Fig. 4c) at 70 K (Fig. 4d). The voltage of CC presents a slight reduction to 197 kV, 2 ms after the fault occurrence (Fig. 4b). This voltage dip can be explained by the fact that the investigated fault is applied close to CC connection point (1 km from Bus 1).

This scenario provides a deeper insight on the influence of R_f on the quenching process. In particular, during highly-resistive faults, fault current is predominantly reduced by the R_f and the quenching process is jeopardized. As the quenching depends on the magnitude of the fault current, the influence of high R_f values introduces a challenge for the detection of highly-resistive faults.

3.3. Scenarios F_3 and F_4

The performance of SC1, SC2 and CC has also been investigated against a solid PP fault applied at 0.1% of CC length (0.06 km from Bus 1). During normal conditions the current flows mainly through SC2 which transmits offshore wind power to AC grid 1. Once the fault occurs, the current flowing through SC1 reaches a peak of 5 kA (Fig. 5a), the voltage of SC1 is reduced to 50 kV (Fig. 5b), R_{eq} reaches the value of 130 Ω (Fig. 5c) and T rises up to 190 K (Fig. 5d). Therefore, it can be observed that the occurrence of a solid fault at CC leads to quenching of SC1. As depicted in Fig. 5a, 15 ms after the fault occurrence, the fault current flowing through SC1 is reduced due to the abrupt increase in R_{eq}. However, the value of R_{eq} and T are retained to 130 Ω and 190 K, respectively. This can be explained considering the time required for SC1 to recover and its T to be reduced below T_C.

The highest the peak value of T during fault, the slowest the recovery process (within the range of few sec to few min) [28]. The recovery time of SCs is determined by the fault parameters, the structure of the SC, the type and efficiency of the cooling system [29].

Furthermore, the presence of a solid PP fault applied at CC leads also to quenching of SC2. The delay in quenching of SC2 is due to the higher value of I_C compared to that of SC1. Specifically, SC2 starts to quench 18 ms after the fault occurrence, presenting a peak of DC current equal to 8.5 kA, R_{eq} of 30 Ω (Fig. 5c) and T equal to 130 K (Fig. 5d). The fault DC current flowing through CC is illustrated in Fig. 5a, while the voltage dip in Fig. 5b.

Furthermore, the simulation results of the permanent PP solid fault at Bus 3, F_4, are shown in Fig. 6. Fig. 6a shows the DC currents flowing through the two SCs and CC. It is observed that for a solid fault at Bus 3 both of SCs quench. Specifically, SC1 quenches 4 ms after the fault occurrence, presenting R_{eq} of approximately 140 Ω (Fig. 6c) and T rise up to 190 K (Fig. 6d). The voltage of SC1 is reduced to 0 kV as it is directly connected to the faulted bus. The DC current flowing through SC1 is sustained to 400 A as the increase in R_{eq} limits the fault current magnitude. The SC2 quenches 8 ms after the fault initiation. The peak of DC current flowing through SC2 is 10 kA (Fig. 6a), while during quenching, as R_{eq} reaches values of 120 Ω (Fig. 6c) the DC current through SC2 is maintained at 5 kA (Fig. 6a). The DC current through CC presents a peak of 3.4 kA (Fig. 6a) and the voltage of CC is decreased to 1.2 kV (Fig. 6b).

Therefore, from the investigation of the external fault at CC and Bus 3, it can be concluded that quenching of SCs can be initiated by external faults, introducing a potential challenge for the stability and coordination of the protection schemes.

3.4. Fault analysis assessment

By summarizing the results obtained during the simulation of the F_1 to F_4 fault scenarios the following key findings from power system protection perspective are worth to be highlighted:
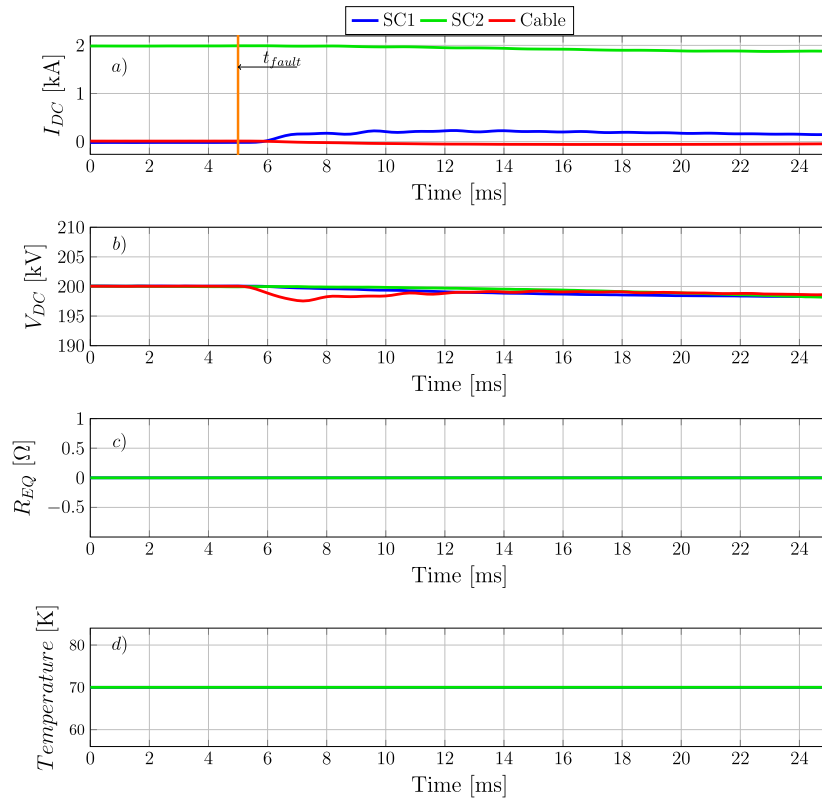
Fig. 4. Highly resistive PP fault at 99% of SC1 length with $R_f = 300 \ \Omega$: (a) SC1, SC2 and CC DC currents, (b) SC1, SC2 and CC DC pole-to-pole voltage, (c) equivalent resistance of SC1 and SC2, (d) temperature of SC1 and SC2.

Fig. 5. Solid PP fault at 0.1% of the CC length: (a) SC1, SC2 and CC DC currents, (b) SC1, SC2 and CC DC pole-to-pole voltage, (c) equivalent resistance of SC1 and SC2, (d) temperature of SC1 and SC2.

Fig. 6. Solid PP fault at Bus 3: (a) SC1, SC2 and CC DC currents, (b) SC1, SC2 and CC DC pole-to-pole voltage, (c) equivalent resistance of SC1 and SC2, (d) temperature of SC1 and SC2.
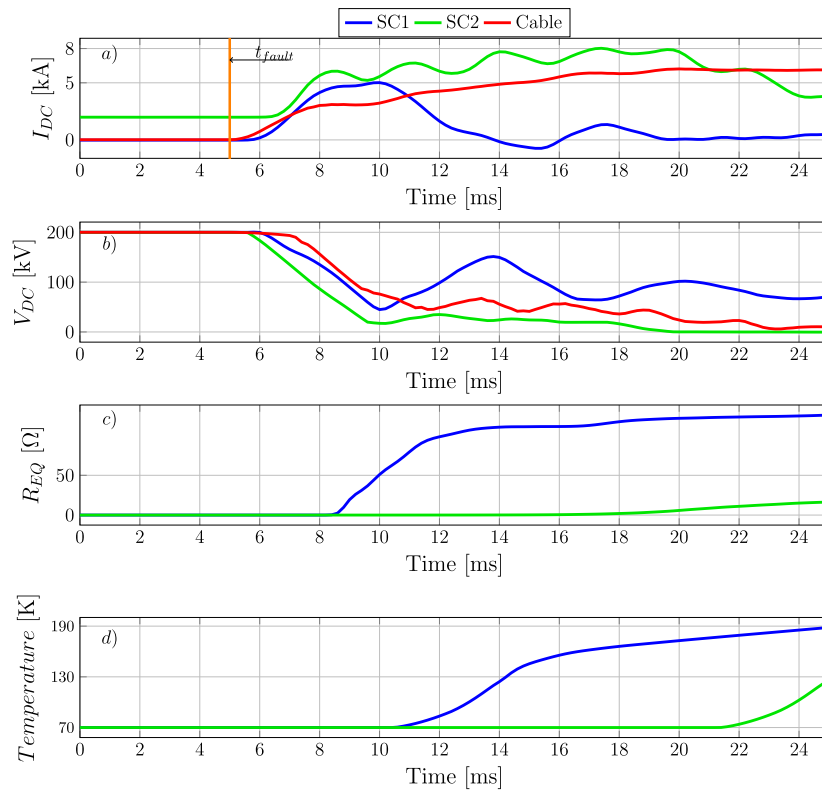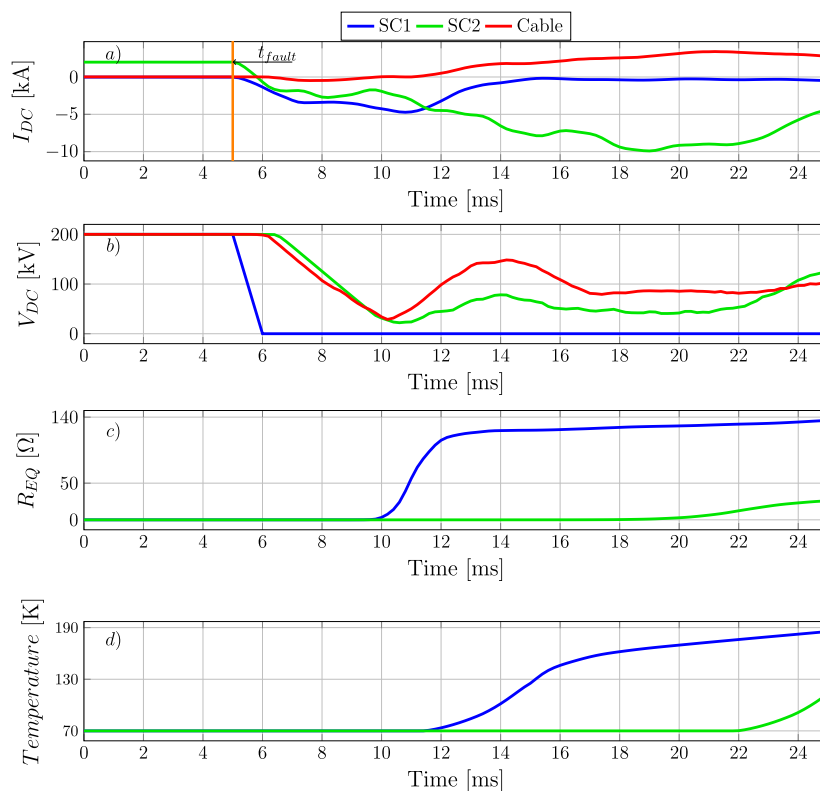
- The variable R_{eq} of the SCs during quenching and the subsequent fault current reduction may cause malfunctions to existing protection schemes. Therefore, these constitute the key factors which should be taken into consideration during the design of more advanced protection solutions.
- For the protection of SCs in meshed HVDC systems schemes with increased sensitivity are required to provide adequate detection of highly-resistive faults, during which the quenching process is compromised, and increased discrimination capability to remain stable against external faults.

3.5. Investigation of derivative-based protection philosophy

This section demonstrates the limitations of existing protection schemes for meshed HVDC systems which incorporate SCs.

Current and voltage derivative-based protection schemes have been widely-proposed in the technical literature for fault detection and location applications for meshed HVDC systems as they present increased sensitivity, speed, accuracy and minimize the need for communication link (i.e., only local measurements are required) [30].

In this work, prior to the analysis of the proposed protection algorithm, the potential of utilizing di/dt and dv/dt based protection has been assessed by conducting a qualification analysis which presents the basic challenges of the threshold-based protection schemes for HVDC systems with SCs, while the further investigation of the settings adjustment is beyond the scope of the presented work. For this purpose, the relay installed at point 3.1 of SC1 (Fig. 1) has been utilized as an indicative test case. For this purpose, the relay operation is based on the local current or voltage measurements captured at point 3.1 of SC1. The protection zone is bounded by the inductive terminations and the current and voltage derivative-based relay should operate only for forward faults (the direction is indicated by the grey arrow in Fig. 1) within the protected zone (no protection directionality has been considered) in order to preserve the protection sensitivity and security.

The value of the current and voltage threshold settings shall be determined considering the protection discrimination requirement between a forward PP internal remote highly-resistive fault (i.e., F_2), during which a tripping signal should be initiated, and a forward PP solid external fault (i.e., F_3), during which the protection scheme should remain stable.

3.6. Scheme based on current derivative

Fig. 7a and b show the di/dt of the current flowing through SC1 measured at the point $P3.1$ during F_2 and F_3, respectively. As it is demonstrated, during F_2, which is a highly-resistive fault with $R_f = 200\ \Omega$, the first di/dt peak is presented 1.2 ms after the fault and is approximately 198 kA/s. During F_3, the first peak of di/dt is approximately 920 kA/s. The magnitude of the peak of di/dt, during F_2, is reduced due to the increase in the variable R_{eq} of SC1 and the high value of R_f.

Effectively, the obtained results indicated that the selection of low current threshold setting is required in order to ensure the detection of internal highly-resistive faults. Conversely, for low current threshold setting, the current derivative-based relay operates for external solid faults applied on the CC. Therefore, this protection philosophy provides a trade-off between the protection sensitivity and stability for meshed HVDC systems with SCs.

3.7. Scheme based on voltage derivative

Fig. 8a and b depict the dv/dt of the voltage signatures captured at the point 3.1 during F_2 and F_3, respectively. It can be noticed that the peak of the dv/dt, during F_2 is approximately 10 MV/s, 2.5 ms after the fault occurrence, while during F_3, the first peak of the dv/dt is 50 MV/s.

Similarly to the case of the current derivative-based relay, the results showed that the selection of low voltage threshold setting is required for the secure operation against internal highly-resistive faults,
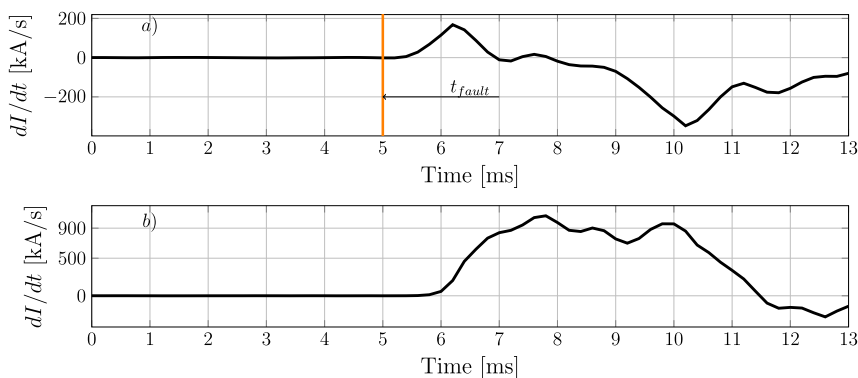
Fig. 7. Results of di/dt during: (a) a PP internal, remote highly-resistive fault at 99% of SC1 length with $R_f = 200\ \Omega$ (b) a PP external solid fault at 0.1% of CC length.
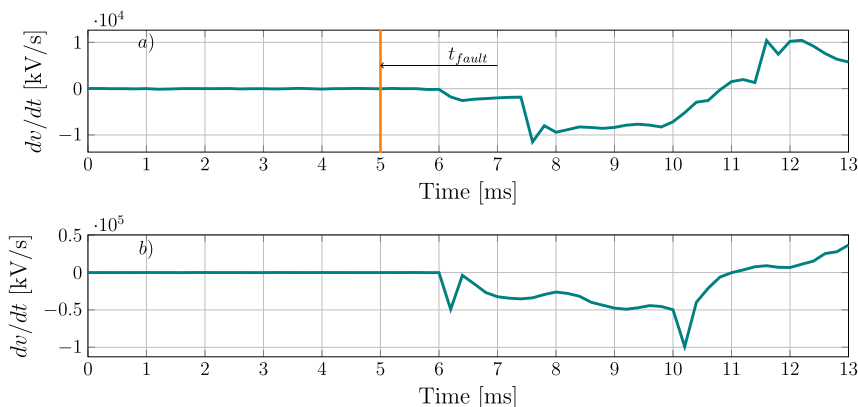

Fig. 8. Results of dv/dt during: (a) a PP internal, remote highly-resistive fault at 99% of SC1 length (b) a PP external solid fault at 0.1% of CC length.

jeopardizing the protection stability against external solid faults applied on the CC. Consequently, it can be concluded that quenching, R_{eq} variations, the increase in R_f and the current limitation have an adverse impact on the proper selection of the voltage threshold setting.

4. Proposed algorithm

The proposed data-driven scheme exploits the advantages of the XGBoost Machine Learning (ML) algorithm for real-time fault detection and classification. In the presented work the fault classification term refers to the identification of the faulted element (i.e., buses, SC1, SC2 and CC).

By utilizing as an indicative example the Bus 3, shown in Fig. 9, the XGBoost-based scheme is a centralized (on substation level) protection philosophy which protects the system against faults occurring within the protected zone, accounting for faults applied on Bus 3 (F_4), SC1 (F_1) and SC2 (F_5). Correspondingly to Bus 3, the same centralized XGBoost-based protection philosophy has been assumed to be installed to the other two buses illustrated in Fig. 1 (Bus 1 and Bus 2). In particular, the XGBoost-based scheme installed at Bus 1 detects and classifies faults occurring at Bus 1, SC1 and CC, while the protected zone of the XGBoost-based scheme installed at Bus 2 includes faults at Bus 2, CC and SC2. The algorithm detects the presence of a fault based on local current and voltage measurements obtained from the cables and the converter attached to the corresponding DC buses and therefore, there is no requirement for communication and measurements transmission among the buses.

The fault is classified in order to determine the faulted element within the protected zone or the presence of an external fault beyond the protected zone. Following the fault classification, a tripping signal is initiated and sent to the corresponding Circuit Breakers (CBs)

to clear the fault. Conversely, during a detected external fault, the XGBoost-based protection remains stable.

For the practical implementation of the proposed scheme, authors devised the design depicted in Fig. 9. Merging Units (MUs) can be installed to acquire the local current and voltage measurements based on the IEC 61869 standard. The MUs perform all data processing, accounting for sampling and digitization and transmit the digital output of the current and voltage signatures to the centralized protection scheme via Ethernet, using the IEC 61850−9−2 protocol. The protection functions are assumed to be implemented within the XGBoost-based scheme, while for the realization of the fault clearance, the initiated tripping signal can be sent to the corresponding CBs via the Generic Object Oriented Substation Event (GOOSE) protocol defined by the IEC 61850 standard. The development of the protection algorithm is thoroughly explained in the following subsections.

4.1. Data generation and acquisition

Initially, with the scope of generating a diverse dataset, several fault scenarios were simulated using the system illustrated in Fig. 1. The system parameters that have been modified during the iterative simulation process include the fault type, fault resistance and fault position. For the resistive faults 20 values of R_f have been considered within the range of 0 Ω to 350 Ω. The maximum fault resistance of 350 Ω has been selected as a typical value for highly resistive faults in HVDC systems as reported in the technical literature [31−34]. Specifically, the initial dataset is composed of 1800 fault scenarios which include PP, PG and NG fault types occurring at every 10% of SC1, SC2 and CC length with 20 values of fault resistance and PP, PG and NG faults with 20 values of fault resistance applied at Bus 1, Bus 2 and Bus 3.

During the simulation studies, pre-fault (5 ms time window) and post-fault (20 ms time window) local current and voltage waveforms
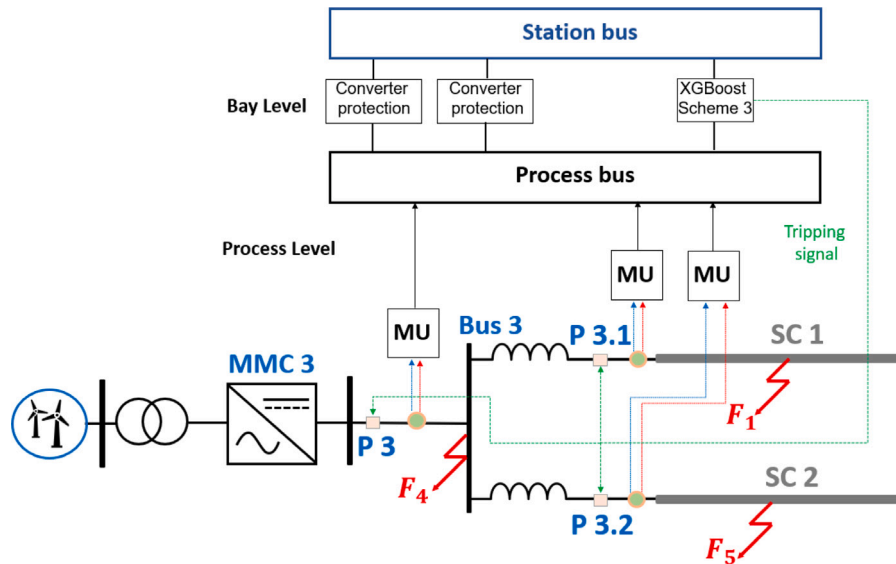
Fig. 9. Overview of the XGBoost-based scheme installed at Bus 3.

(at substation level) were measured at one terminal of cables, the DC side of converter and the corresponding bus. The generated signals have been captured with sampling frequency of 20 kHz [3].

4.2. Data pre-processing

One of the main advantages of the tree-based algorithms, such as the XGBoost model, compared to other AI techniques, is the low requirements on the data preparation [35]. Therefore, there is no need for extensive pre-processing of the obtained voltage and current signatures.

The final Python-based dataset has been formed based on the captured time-domain current and voltage measurements, without considering other features (i.e., current derivative, voltage derivative etc.) or transformations (i.e., Wavelet Transform). Prior to the training of the developed algorithm, the dataset was split into smaller datasets. Specifically, 80% of the initial dataset was used for the training, while the remaining 20% for the testing of XGBoost model. It should be noted that the XGBoost algorithm has the capability to perform internal Cross-Validation (CV), hence it is not necessary to create a separate validation dataset.

4.3. Multi-class classification

The acquired time-domain current and voltage measurements are used as inputs to the XGBoost-based scheme, to detect the presence of a fault and identify the faulted element. During the training process the voltage and current measurements have been contaminated with random white noise in order to represent the possible impact of the noisy measurements on the fault detection and classification. Specifically, random noise within the range of 80 to 130 signal-to-noise ratio (SNR) has been added to the training dataset.

In the presented work the fault detection and discrimination functions have been formed as a multi-class classification problem. Specifically, for the scheme installed at Bus 3 (Fig. 9) (which is the centralized proposed scheme), XGBoost classifier initiates output }}1ε, indicating faults at SC1, }}2ε indicating faults at SC2 and }}3ε for faults at Bus 3. Conversely, when the XGBoost output is }}0ε, the presence of an external fault beyond the protected zone is identified. The correspondence between the predicted classes and the faulted element for the developed XGBoost-based scheme installed at Bus 3 is given in Table 4:

Effectively, during an internal fault, the generated output of the XGBoost classifier is utilized as a tripping signal which is sent to

Table 4
Correspondence between predicted class and fault type for the developed XGBoost-based scheme installed at Bus 3.

XGBoost-based scheme	Class	Fault
	1	at SC1
at Bus 1	2	at CC
	3	at Bus 1
	0	external

the corresponding CB for the isolation of the faulted element. Contrarily, no tripping signal is initiated during the identified external faults. Fig. 10 shows an overview of the developed XGBoost-based fault detection–classification philosophy.

4.3.1. XGBoost algorithm for multi-class classification

XGBoost algorithm is a decision tree-based ensemble model based on gradient boosting which is designed to be very efficient and easily applicable in fault management application with tabular data [35]. The state-of-the-art XGBoost classifiers are very flexible and robust algorithms for complex classification problems as they combine the advantages of the tree-based ML algorithms with lower computational complexity and hence higher computational speed [36]. In particular, XGBoost operation depends on the modelling of tree algorithms, selecting different features of the initial dataset and creating the conditional nodes. The boosting term refers to an ensemble ML method according to which weak learners are trained sequentially and combined to build a stronger learner with better predictive performance. Based on the main principles of the Gradient Boosting (GBM) framework, which consists the core of the XGBoost algorithm, during the training process each weak learner tries to eliminate the weaknesses of its predecessor, resulting in strong learners with high degree of accuracy.

The operation of the XGBoost algorithm is dependent on the minimization of the objective function given by (7), using gradient descent:

$$Obj = \sum_{n}^{i=1} l(y_i, \hat{y}_i^{(t-1)} + f_t(x_i)) + \Omega(ft) \tag{7}$$

where l is the loss function which represents how well the model fits on the training dataset, $\hat{y}_i^{(t-1)}$ is the previous model at $t-1$, $f_t(x_i)$ is the new model and $\Omega(ft)$ represents the regularization function which measures the complexity of the trees.
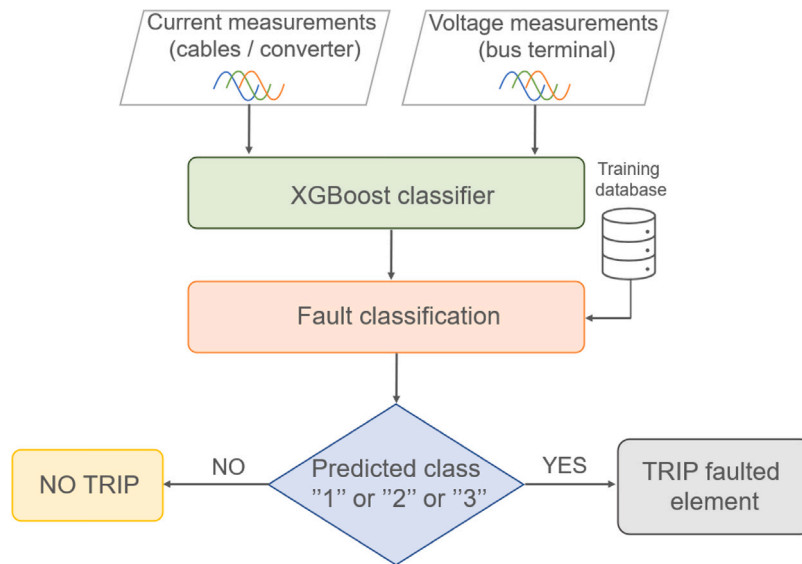
Fig. 10. Overview of the XGBoost-based algorithm.

There many comparative analyses reported in literature which highlight the advantages of XGBoost algorithm over other classifiers. Particularly, authors in [37], demonstrate that XGBoost algorithm is a scalable ensemble technique which outperforms gradient boosting and random forests classifiers in terms of accuracy and computational speed. The work conducted in [38,39] indicate that XGBoost algorithm provides higher degree of accuracy compared to ANN and SVM classifiers, respectively, while concurrently reduces the execution time and the computational complexity. The superiority of XGBoost algorithm for classification problems over ANN algorithms is reported in [40]. Specifically, the comparative analysis showed that XGBoost achieved higher accuracy on the testing data and performed the entire classification process within 30 min, conversely ANN model required 15 h to complete the entire classification process and provided lower accuracy on the testing dataset. Furthermore, ANN models require extensive tuning both, in parameters and model architecture, while XGBoost algorithm performs well without extensive parameters tuning. The unique features of XGboost algorithm for fault diagnosis problems are presented in [35,41–43] and the studies revealed that XGBoost algorithm is a robust, computationally efficient algorithm which presents faster and more accurate results over other ML model such as Long–Short Term Memory (LSTM) model and traditional neural network models. The main advantages offered by the XGBoost algorithm are listed as follows and showcase the superiority of the selected algorithm compared to other classification models:

- Fastest implementation of the GBM tree-based algorithms [38].
- Higher efficiency compared to conventional artificial neural network classifiers [36].
- Incorporates randomization techniques (i.e., random subsample), reducing the over-fitting on the training dataset and presenting enhanced generalization capability [44].
- Utilizes the power of the parallel computation to construct trees resulting in less computational time and faster training process [40].
- Achieves state-of-the-art results with tabular data [45].

Therefore, the XGBoost algorithm combines efficiency, operational speed and increased generalization capability which are attributes very important for the fault management problems.

In the presented work, in order to select the XGBoost model with the best prediction performance, hyperparameter tuning was performed prior to the commencement of the actual learning process [25]. For this

Table 5
Simulation scenarios.

Hyperparameter	Value
Booster	gbtree
Alpha	10
Number of estimators	200
Lambda	1
Maximum tree depth	3
Learning rate	0.1

purpose, the training dataset was divided into 5-folds ($k = 5$) and each combination of hyperparameters is subjected to the 5-fold CV for the determination of the optimum combination. The 5-fold CV has been implemented based on the "GridSearchCV" scikit-learn class and as CV score the F1-score was selected. All the experiments were executed using AMD Ryzen™ 9 5900HX (16-core/12-thread, 16 GB cache, up to 4.0 GHz max boost) processor. The optimum hyperparameters of the developed XGBoost-based scheme are presented Table 5.

4.4. XGBoost-based scheme time delays

Prior to the testing of the developed scheme, for the realistic implementation all the anticipated time delays within the DC substation should be identified. The expected total operating time of the XGBoost scheme, t_{op}, is calculated based on (8) and consists of time delays associated with the data processing, t_d, (including measurements digitization and communication) and the XGBoost algorithm execution, $t_{XGBoost}$, (time required for the algorithm to provide the output signal):

$$t_{op} = t_d + t_{XGBoost} \tag{8}$$

The developed protection philosophy at each bus is based on current and voltage measurements from all the cables and the converter attached to the corresponding DC bus. Considering the use of MUs as illustrated in Fig. 9 and an Ethernet switch for realization of IEC-61850, the maximum anticipated time delay, t_d is given by (9):

$$t_d = t_s + t_{MU} + t_{Eth} + t_{pp} \tag{9}$$

where t_s denotes the maximum time delay resulting from the analogue sampling (i.e., $t_s = 50$ μs); t_{MU} is the time required to encode the sampled values in the MUs and can be estimated to 12 μs according to [46]; t_{Eth} is the maximum time delay imposed by the Ethernet link latency and is estimated to 6.34 μs based on [2] and t_{pp} is 9.5 μs,
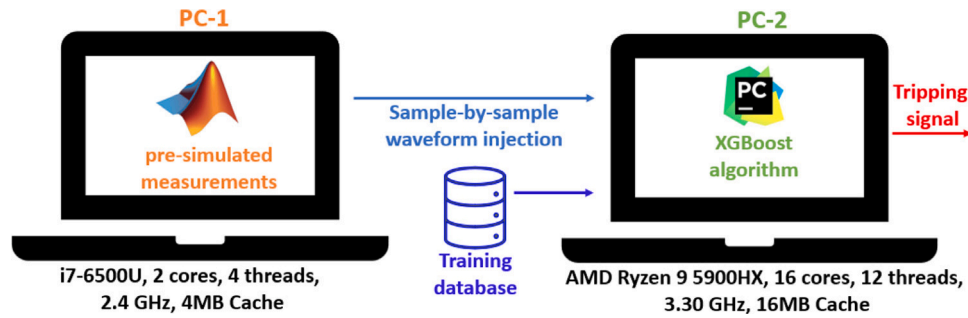
Fig. 11. Overview of SIL testing environment used for time performance assessment of the XGBoost-based scheme.

Table 6
XGBoost confusion matrix for train–test split percentage of 80%–20%.

Actual/predicted condition	Predicted negative	Predicted positive
Actual negative	TN = 96%	FP = 0.5%
Actual positive	FN = 3%	TP = 98%

Table 7
XGBoost confusion matrix for train–test split percentage of 65%–35%.

Actual/predicted condition	Predicted negative	Predicted positive
Actual negative	TN = 85%	FP = 3%
Actual positive	FN = 11%	TP = 90%

Table 8
XGBoost confusion matrix for train–test split percentage of 50%–50%.

Actual/predicted condition	Predicted negative	Predicted positive
Actual negative	TN = 78%	FP = 4%
Actual positive	FN = 27%	TP = 86%

relying on the work conducted in [46], and refers to the maximum time required for the protection system to decode the sampled values. The total t_d is 77.84 μs.

Finally, the time delay associated with the XGBoost algorithm, $t_{XGBoost}$, is determined by many factors accounting for coding efficiency and the power of the processing system. The total t_{op} of the proposed scheme will be assessed experimentally in the following section.

5. Simulation results and validation of the XGBoost-based scheme

The effectiveness and the generalization capability of the XGBoost scheme have been validated using proper evaluation metrics and time assessment studies. Initially, the ability of the developed scheme to detect and classify correctly different faults was evaluated on the testing dataset, considering the F1-score as evaluation metric. Furthermore, time performance assessment studies were carried out using a SIL testing platform in order to validate the suitability of the proposed scheme for real-time implementation. Additionally, the performance of the algorithm has been tested against the addition of white noise in voltage and current time-domain signals, emulating potential effects arisen by measurement-related noise.

5.1. F1-score evaluation

F1-score is a widely used evaluation metric in ML applications. In particular, F1-score provides a combination between the precision and recall evaluation metrics, considering the impact of both, the False Positive (FP) predictions and the False Negative (FN) predictions, respectively. The XGBoost classifier was tested using 20% of the initial dataset. The split of the initial dataset to 80% for training and the remaining 20% for testing it is a common practice utilized in ML applications [47]. Table 6 shows the normalized confusion matrix generated during the testing process.

As concluded by Table 6, the high percentage of True Positive (TP) predictions, confirms the capability of the developed scheme to detect and classify correctly the faults within the protected zone, while the increased value of the True Negative (TN) percentage indicates the stability of the algorithm against the external faults. Regarding the percentage of FP, which indicate the falsely initiation of the tripping signal for an external fault and the FN percentage which refers to the failure of tripping signal initiation for an internal fault, both are very low, validating the high degree of protection reliability and dependability. The total F1-score is calculated based on (10). Deriving the values from

the confusion matrix presented in Table 6 the final value of the F1-score is 98%.

$$F1 - score = 2 \cdot \frac{Recall \cdot Precision}{Recall + Precision} = \frac{TP}{TP + \frac{1}{2} \cdot (FN + FP)} \qquad (10)$$

5.2. Sensitivity analysis regarding train–test dataset split

In this sub-section a sensitivity analysis was performed with respect to the train–test split percentages in order to evaluate the initial selection (80% of initial dataset for training and the remaining 20% for testing) and investigate its impact on the performance of XGBoost model. For this purpose, the developed XGBoost model was tested on 35% of the initial dataset (the remaining 65% was utilized for training) and 50% of the initial dataset (the remaining 50% was utilized for training). Similarly, to sub-Section 5.1 the evaluation was performed based on F1-score.

Tables 7 and 8 present the normalized confusion matrices generated during the testing process on 35% and 50% of the initial dataset, respectively.

The resulting F1-score for train–test split percentage of 65 %–35 % is 92% and for train–test split percentage of 50 %–50 % is 84%. Therefore, it can be concluded that as the percentage of the initial dataset utilized for training is reduced and thus the training set representativeness decreases, the resulting F1-score decreases as well. Specifically, as the percentage of the initial dataset assigned to training process is reduced, the percentage of FP predictions increases, resulting in the falsely initiation of the tripping signal for faults beyond the protected zone, diminishing protection security. An increase it is also observed in the percentage of FN percentage, which indicates the failure of tripping signal initiation, jeopardizing the protection dependability and reliability. Conversely, as the percentage of the initial dataset utilized for training decreases, the resulting percentages of TP and TN predictions are reduced, affecting the protection sensitivity and stability, respectively. Based on the obtained results the XGBoost model trained of 80% of the initial dataset was selected for the presented studies.
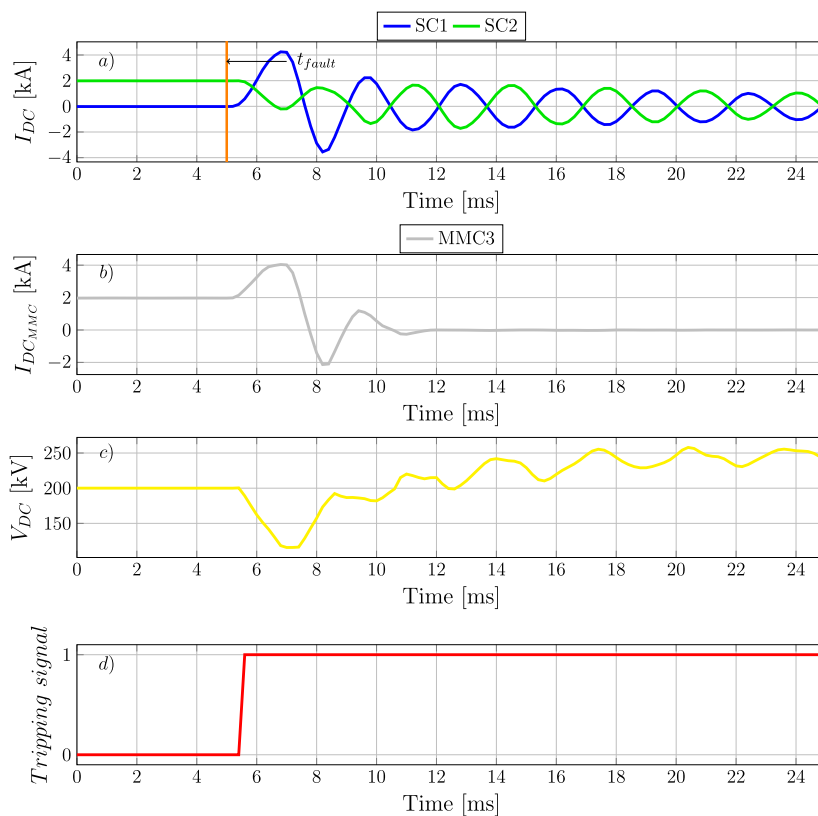
Fig. 12. Overview of SIL testing environment used for time performance assessment of the XGBoost-based scheme.

5.3. Software in the loop testing for real-time validation

This subsection presents the results of the real-time assessment of the XGBoost-based scheme installed at Bus 3, considering realistic digital infrastructure. The ultimate goal is to acquire a deeper insight of the time response of the proposed scheme and validate its performance for real-time implementation. On that front, the performance of XGBoost-based scheme at Bus 3 (illustrated in Fig. 9) was tested with respect to time required for the initiation of the tripping signal. The assessment was conducted utilizing the testing environment in Fig. 11, which forms a real-time SIL platform. Similarly, real-time SIL time performance evaluation could be carried out for the XGBoost schemes installed at Bus 1 and Bus 2.

A variety of fault scenarios were simulated utilizing the network depicted in Fig. 1, and the corresponding voltage and current measurements were extracted for post-processing. The simulated database was stored in PC-1 and the waveforms were injected sample-by-sample to PC-2 through TCP/IP sockets configuration. The final trained model of XGBoost algorithm was stored in PC-2 in order to generate the tripping signal. The specifications of PC-1 and PC-2 are presented in Fig. 11.

Indicatively, Fig. 12 shows the simulation results of a PP solid fault applied at 58% of the SC1 length, at $t = 5$ ms, which quantifies the time performance of the XGBoost-based scheme installed at Bus 3. Fig. 12a to Fig. 12c illustrate the utilized voltage and current measurements, accounting for the currents measured at the terminal P3.1 of SC1 and P3.2 of SC2 (Fig. 12a) and the DC side of MMC3 converter (Fig. 12c) and the DC voltage at Bus 3. It is evident that the fault is detected by the proposed scheme and the corresponding tripping signal is initiated approximately 0.5 ms after the fault occurrence (Fig. 12d).

Furthermore, during the real-time SIL testing, the performance of XGBoost-based scheme installed at Bus 3 was evaluated on 200 additional, previously unseen fault scenarios (the fault location and the R_f are not part of the initial dataset). The principal objective of this assessment is to further validate the generalization capability of the

proposed scheme against measurements which are not part of the training or testing datasets. Some of the results are presented in Table 9 and establish the effectiveness of the proposed protection philosophy. Specifically, the proposed scheme detects and classifies correctly the faults within the protected zone (i.e., faults applied on SC1, SC2 and Bus 3) and provide the corresponding tripping signal (even during highly-resistive faults). Conversely, the scheme remains stable against external faults (faults applied on CC, Bus 1 and Bus 2) which belong to the protected zones of XGBoost schemes installed at Bus 1 and Bus 2. Regarding the operation time, which is of paramount importance in HVDC systems, the tripping signal is initiated within the time range of 0.0582 ms to 1.3104 ms, providing an average time of 0.2912 ms. Therefore, it can be concluded that the proposed scheme fulfils all the requirements of an effective protection solution for meshed HVDC systems with SCs, accounting for increased discrimination, security, stability and operation speed.

5.4. Impact of noise

The analysis presented in this subsection investigates the impact of white noise on the performance of the proposed scheme. During the practical deployment of the developed protection algorithm in meshed HVDC systems with SCs, unwanted distortion may be introduced within the measurements, emanating from quality issues, sensing and measuring equipment. Therefore, to de-risk the proposed scheme and validate its effectiveness under such conditions, the time-domain current and voltage signatures of the testing scenarios, investigated in Section 5.3, have been contaminated with artificial noise. Fig. 13 shows the fault current and voltage signatures of Fig. 12 after the addition of artificial noise (SNR = 30 dB).

It is worth reiterating that the XGBoost-based scheme has been trained on data with random noise within the range of 80 to 100 SNR. The presented results aim to confirm the generalization capability and

Table 9

Time performance of XGBoost scheme installed at Bus 3 during previously unseen fault scenarios.

Faulted element	Fault type	Rf [Ω]	Location %	t_{op} [ms]	Faulted element	Fault type	Rf [Ω]	Location %	t_{op} [ms]
SC1	PP	0	0.50	0.0898	Bus 1	PP	0	–	NO TRIP
		2	15	0.0988			2	–	NO TRIP
		5	45	0.1091			5	–	NO TRIP
		50	65	0.1591			50	–	NO TRIP
		300	99	0.2018			300	–	NO TRIP
		0	87	0.0988			45	–	NO TRIP
		100	1	0.1068			10	–	NO TRIP
	PG	0	0.20	0.0901		Positive PG	0	–	NO TRIP
		1	1.4	0.0951			1	–	NO TRIP
		10	32	0.0908			10	–	NO TRIP
		30	74	0.1009			30	–	NO TRIP
		350	98.90	1.0890			350	–	NO TRIP
		2	92	0.1073			100	–	NO TRIP
		95	20	1.0113			4	–	NO TRIP
	NG	0	1	0.0938		NG	0	–	NO TRIP
		3	13	0.0920			3	–	NO TRIP
		15	25.60	0.0901			15	–	NO TRIP
		25	58.90	0.1256			25	–	NO TRIP
		1	0.05	0.0582			1	–	NO TRIP
		0	97	1.0982			200	–	NO TRIP
		100	98	0.1911			67	–	NO TRIP
SC2	PP	0	2	0.0997	Bus 2	PP	0	–	NO TRIP
		2	17	0.0988			2	–	NO TRIP
		5	38	0.1003			5	–	NO TRIP
		50	49.50	0.1024			50	–	NO TRIP
		300	64.90	0.1109			300	–	NO TRIP
		350	12.5	0.1219			11	–	NO TRIP
		3	75.2	0.9876			88	–	NO TRIP
	PG	0	8	0.0956		PG	0	–	NO TRIP
		1	21	1.0841			1	–	NO TRIP
		10	37	1.0943			10	–	NO TRIP
		30	44.20	1.0928			30	–	NO TRIP
		100	21.2	1.0867			35	–	NO TRIP
		350	92	1.2341			350	–	NO TRIP
		0	99	0.0431			16	–	NO TRIP
	NG	0	49.80	0.0998		NG	0		NO TRIP
		3	59	0.1023			3	–	NO TRIP
		15	81	0.1025			15	–	NO TRIP
		25	69.90	0.1037			25	–	NO TRIP
		200	96	1.0984			200	–	NO TRIP
		90	13.5	1.1014			100	–	NO TRIP
		0	93.8	1.0004			1	–	NO TRIP
Bus 3	PP	0	–	0.0827	CC	PP	0	0.89	NO TRIP
		2	–	0.0838			2	12	NO TRIP
		5	–	0.0889			5	48	NO TRIP
		50	–	0.0908			50	67	NO TRIP
		1	–	0.0887			100	0.4	NO TRIP
		300	–	0.0907			300	99	NO TRIP
		100	–	1.3104			1	88	NO TRIP
	PG	0	–	0.0813		PG	0	3	NO TRIP
		1	–	0.0921			1	18	NO TRIP
		10	–	0.0942			10	47	NO TRIP
		30	–	0.1022			30	85.3	NO TRIP
		350	–	0.1030			350	91	NO TRIP
		0.5	–	0.0532			100	11.1	NO TRIP
		60	–	0.1702			2	76.7	NO TRIP
	NG	0	–	0.0803		NG	0	2	NO TRIP
		3	–	0.1012			3	27	NO TRIP
		15	–	0.0989			15	58	NO TRIP
		25	–	0.0832			25	76.7	NO TRIP
		100	–	0.1355			100	18.2	NO TRIP
		200	–	0.1540			200	98.8	NO TRIP
		2	–	0.0849			2	5.6	NO TRIP

the time response of the proposed scheme under the influence of wider range of white noise.

The final results are presented in Table 10 and show the maximum and the average tripping time, t_{op}, of the XGBoost-based scheme installed at Bus 3. From the resulting time values it is evident that as the noise level increases (the value of the SNR decreases), the value of the t_{op} remains approximately the same.

In more specific, for the detection of the faults on SC1, the maximum t_{op} is 1.0982 ms for SNR 100 dB. For the same SNR, the average t_{op} is 0.2416 ms, while for SNR 30 dB, the maximum t_{op} is 1.0981 ms and the average t_{op} is 0.2412 ms. It is evident that an increase in the additive noise causes a minor change in the operation speed of the XGBoost-based scheme. The same trend is presented in the detection of faults on SC1 and Bus 3. Furthermore, the proposed scheme remains stable
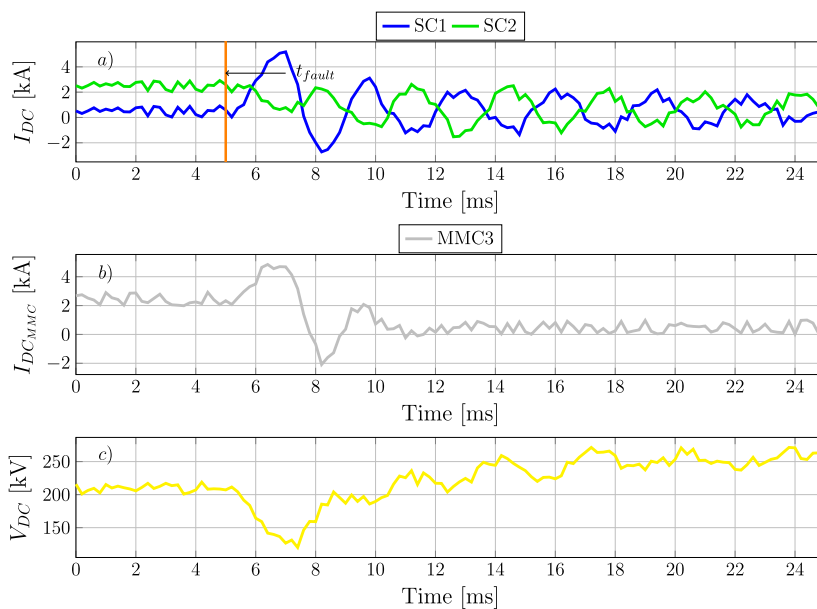
Fig. 13. Current and voltage measurements after the addition of 30 dB noise.

Table 10
Time performance of XGBoost-based scheme considering artificial noise to current and voltage measurements of the testing scenarios.

SNR [dB]	SC1		SC2		Bus 3		Bus 1		Bus 2		CC	
	t_{op} max [ms]	t_{op} avg [ms]	t_{op} max [ms]	t_{op} avg [ms]	t_{op} max [ms]	t_{op} avg [ms]	t_{op} max [ms]	t_{op} avg [ms]	t_{op} max [ms]	t_{op} avg [ms]	t_{op} max [ms]	t_{op} avg [ms]
∞	1.0982	0.2416	1.2341	0.3513	0.1543	0.0952	NO TRIP	NO TRIP	NO TRIP	NO TRIP	NO TRIP	NO TRIP
100	1.0983	0.2415	1.2341	0.3513	0.1543	0.0952	NO TRIP	NO TRIP	NO TRIP	NO TRIP	NO TRIP	NO TRIP
80	1.0983	0.2415	1.2341	0.3512	0.1543	0.0951	NO TRIP	NO TRIP	NO TRIP	NO TRIP	NO TRIP	NO TRIP
60	1.0983	0.2414	1.2341	0.3512	0.1541	0.0949	NO TRIP	NO TRIP	NO TRIP	NO TRIP	NO TRIP	NO TRIP
30	1.0981	0.2412	1.2339	0.3510	0.1538	0.0944	NO TRIP	NO TRIP	NO TRIP	NO TRIP	NO TRIP	NO TRIP

during faults on CC and Bus 1 and Bus 2. Therefore, it is inferred that the performance of the developed scheme is not jeopardized by the addition of the white noise.

6. Conclusions

In the presented work a novel centralized fault detection and classification scheme is proposed for the protection of multi-terminal HVDC grids with SCs. The developed scheme utilizes the principles of the XGBoost ML algorithm and protects the system against faults occurring along the cables (SC and CC) and the buses.

The deployment of the SCs has introduced many fault-related challenges within the networks due to the quenching phenomenon and renders the fast and accurate fault detection and classification a very challenging task. The limitations of the existing DC protection schemes, such as the derivative-based schemes, in conjunction with the ever-increasing availability of data in the future power grids offer the opportunity for innovative protection solutions.

The proposed XGBoost-based scheme has been found to provide adequate protection for different fault types, location and resistances. The results from the real-time SIL testing validate the fast and accurate fault detection and classification under various fault conditions and consequently highlight the applicability of the developed scheme for real-time implementation. Specifically, the results showed that the operation time lies within the range of 0.0803 ms and 1.2341 ms, which complies with the protection requirements for HVDC grids. Furthermore, the XGBoost-based algorithm presents increased discrimination capability by initiating a fast tripping signal during the highly-resistive internal faults and remaining stable during external faults. Additionally, the generalization capability of the proposed scheme has been

tested under the influence of white noise. The results verified the robust performance of the XGBoost-based scheme on the noisy measurements. Overall, the proposed scheme is suitable for the detection and classification of faults in HVDC grids with SCs, and hence can be considered a very promising solution for the implementation of fast and reliable DC bus and SCs protection. Following the successful development and evaluation of the proposed centralized XGBoost-based scheme, more research shall be steered towards the simultaneous assessment of the three centralized XGBoost-based schemes installed at Bus 1, Bus 2 and Bus 3 along with the investigation of back-up protection schemes.

CRediT authorship contribution statement

Eleni Tsotsopoulou: Conceptualization, Methodology, Investigation, Formal analysis, Validation, Writing – original draft. **Xenofon Karagiannis:** Software, Methodology, Writing – review & editing. **Theofilos Papadopoulos:** Methodology, Investigation, Supervision, Writing – review and editing. **Andreas Chrysochos:** Methodology, Investigation, Supervision, Writing – review & editing. **Adam Dyśko:** Supervision, Writing – review & editing. **Dimitrios Tzelepis:** Methodology, Supervision, Writing – review & editing.

Declaration of competing interest

The authors declare that they have no known competing financial interests or personal relationships that could have appeared to influence the work reported in this paper.

Data availability

Data will be made available on request.

References

[1] Yang S, Xiang W, Lu X, Zuo W, Wen J. An adaptive reclosing strategy for MMC-HVDC systems with hybrid DC circuit breakers. IEEE Trans Power Del 2020;35(3):1111–23. http://dx.doi.org/10.1109/TPWRD.2019.2935311.

[2] Tzelepis D, et al. Centralised busbar differential and wavelet-based line protection system for MTDC grids, with practical IEC-61869-compliant measurements. IET Gener Transm Distrib 2018;12(14):3578–86.

[3] Tzelepis D, et al. Single-ended differential protection in MTDC networks using optical sensors. IEEE Trans Power Del 2017;32(3):1605–15. http://dx.doi.org/10.1109/TPWRD.2016.2645231.

[4] CWA3/B434. Technical requirements and specifications of state-of-the-art HVDC switching equipment. CIGRE Technical Brochure 683, Paris; 2017.

[5] Mitra B, Chowdhury B, Willis A. Protection coordination for assembly HVDC breakers for HVDC multiterminal grids using wavelet transform. IEEE Syst J 2020;14(1):1069–79. http://dx.doi.org/10.1109/JSYST.2019.2922645.

[6] Wang Y, et al. Design and experimental research on self-shielding DC HTS cable model with large current capacity. IEEE Trans Appl Supercond 2019;29(5):1–5. http://dx.doi.org/10.1109/TASC.2019.2906277.

[7] Zhou Q, Yang Y, Wang J, Wang L. Analysis and methods for HTS DC cables. IEEE Trans Appl Supercond 2021;31(8):1–3. http://dx.doi.org/10.1109/TASC.2021.3108738.

[8] Li P, Jovcic D, Hodge E, Fitzgerald J. Analysis of bidirectional 15 MW current source DC/DC converter for series-connected superconducting-based 1 GW/100 kV offshore wind farm. Electr Power Syst Res 2022;202:107618. http://dx.doi.org/10.1016/j.epsr.2021.107618.

[9] Zhang D, et al. Testing results for the cable core of a 360 m/10 kA HTS DC power cable used in the electrolytic aluminum industry. IEEE Trans Appl Supercond 2013;23(3):5400504. http://dx.doi.org/10.1109/TASC.2012.2236812.

[10] Ballarino A, et al. The BEST PATHS project on MgB2 superconducting cables for very high power transmission. IEEE Trans Appl Supercond 2016;26(3):1–6. http://dx.doi.org/10.1109/TASC.2016.2545116.

[11] Yamaguchi S, Koshizuka H, Hayashi K, Sawamura T. Concept and design of 500 meter and 1000 meter DC superconducting power cables in Ishikari, Japan. IEEE Trans Appl Supercond 2015;25(3):1–4. http://dx.doi.org/10.1109/TASC.2015.2390045.

[12] Sytnikov V, Kashcheev A, Dubinin M, Karpov V, Ryabin T. Test results of the full-scale HTS transmission cable line (2.4 Km) for the St. Petersburg project. IEEE Trans Appl Supercond 2021;31(5):1–5. http://dx.doi.org/10.1109/TASC.2021.3063067.

[13] Doukas DI, Syrpas A, Labridis DP. Multiterminal DC transmission systems based on superconducting cables feasibility study, modeling, and control. IEEE Trans Appl Supercond 2018;28(4):1–6. http://dx.doi.org/10.1109/TASC.2018.2806081.

[14] Malek B, Johnson BK. Branch current control on a superconducting DC grid. IEEE Trans Appl Supercond 2013;23(3):5401005. http://dx.doi.org/10.1109/TASC.2012.2236813.

[15] Xiang W, et al. Fault transient study of a meshed DC grid with high-temperature superconducting DC cables. IEEE Trans Power Del 2022;1. http://dx.doi.org/10.1109/TPWRD.2022.3177406.

[16] Chen ZH, Jin JX, Zheng LH, Wu ZH. Advanced HTS DC transmission with self-protection function. IEEE Trans Appl Supercond 2016;26(7):1–5. http://dx.doi.org/10.1109/TASC.2016.2594810.

[17] Zhang Z, Venuturumilli SH, Zhang M, Yuan W. Supercondcuting cables-network feasibility study work package 1. 2016.

[18] Faria da Silva F. Comparison of Bergeron and frequency-dependent cable models for the simulation of electromagnetic transients. In: 2016 51st international universities power engineering conference. 2016, p. 1–6. http://dx.doi.org/10.1109/UPEC.2016.8114048.

[19] Hajiri G, Berger K, Dorget R, Lévêque J, Caron H. Thermal and electromagnetic design of DC HTS cables for the future French railway network. IEEE Trans Appl Supercond 2021;31:5400208. http://dx.doi.org/10.1109/TASC.2021.3059598.

[20] SuperPower. SuperPower 2G HTS wire specifications. 2013, URL https://www.superpower-inc.com/specification.aspx.

[21] Tsotsopoulou E, et al. Advanced fault location scheme for superconducting cables based on deep learning algorithms. Int J of Electr Power and Energy Syst 2022;25. http://dx.doi.org/10.1016/j.renene.2021.07.085.

[22] Bruzek C, et al. 6 - using superconducting DC cables to improve the efficiency of electricity transmission and distribution networks: An overview. In: Rey C, editor. Superconductors in the power grid. Woodhead publishing series in energy, Woodhead Publishing; 2015. p. 189–224. http://dx.doi.org/10.1016/B978-1-78242-029-3.00006-6.

[23] Solovyov M, Pardo E, Šouc J, Gömöry F, Skarba M, Konopka P, Pekarčíková M, Janovec J. Non-uniformity of coated conductor tapes. Supercond Sci Technol 2013;26(11):115013. http://dx.doi.org/10.1088/0953-2048/26/11/115013.

[24] Hajiri G, Berger K, Dorget R, Lévêque J, Caron H. Design and modelling tools for DC HTS cables for the future railway network in France. Supercond Sci Technol 2022;35(2):024003. http://dx.doi.org/10.1088/1361-6668/ac43c7.

[25] Tsotsopoulou E, et al. Time-domain protection of superconducting cables based on artificial intelligence classifiers. IEEE Access 2022;10:10124–38. http://dx.doi.org/10.1109/ACCESS.2022.3142534.

[26] Jin T, et al. Measurement of boiling heat transfer coefficient in liquid nitrogen bath by inverse heat conduction method. J Zhejiang Univ Sci A 2009;10:691–6. http://dx.doi.org/10.1631/jzus.A0820540.

[27] Ametani A. A general formulation of impedance and admittance of cables. IEEE Trans Power App Syst 1980;PAS-99(3):902–10.

[28] de Sousa WTB, Shabagin E, Kottonau D, Noe M. An open-source 2D finite difference based transient electro-thermal simulation model for three-phase concentric superconducting power cables. Supercond Sci Technol 2020;34(1):015014. http://dx.doi.org/10.1088/1361-6668/abc2b0.

[29] Yazdani-Asrami M, Seyyedbarzegar S, Sadeghi A, de Sousa WTB, Kottonau D. High temperature superconducting cables and their performance against short circuit faults: current development, challenges, solutions, and future trends. Supercond Sci Technol 2022;35(8):083002. http://dx.doi.org/10.1088/1361-6668/ac7ae2.

[30] Pérez-Molina MJ, Larruskain DM, Eguía P, Valverde Santiago V. Local derivative-based fault detection for HVDC grids. IEEE Trans Appl Supercond 2022;58(2):1521–30.

[31] Blond SL, Bertho R, Coury D, Vieira J. Design of protection schemes for multi-terminal HVDC systems. Renew Sustain Energy Rev 2016;56:965–74. http://dx.doi.org/10.1016/j.rser.2015.12.025.

[32] Li C, Gole AM, Zhao C. A fast DC fault detection method using DC reactor voltages in HVdc grids. IEEE Trans Power Del 2018;33(5):2254–64. http://dx.doi.org/10.1109/TPWRD.2018.2825779.

[33] Lan T, Li Y, Duan X. High fault-resistance tolerable traveling wave protection for multi-terminal VSC-HVDC. IEEE Trans Power Del 2021;36(2):943–56. http://dx.doi.org/10.1109/TPWRD.2020.2998158.

[34] Zheng X, Nengling T, Guangliang Y, Haoyin D. A transient protection scheme for HVDC transmission line. IEEE Trans Power Del 2012;27(2):718–24. http://dx.doi.org/10.1109/TPWRD.2011.2179321.

[35] Stefanidou-Voziki P, Cardoner-Valbuena D, Villafafila-Robles R, Dominguez-Garcia J. Data analysis and management for optimal application of an advanced ML-based fault location algorithm for low voltage grids. Int J Electr Power and Energy Syst 2022;142:108303. http://dx.doi.org/10.1016/j.ijepes.2022.108303.

[36] Bhatnagar M, Yadav A, Swetapadma A. Enhancing the resiliency of transmission lines using extreme gradient boosting against faults. Electr Power Syst Res 2022;207:107850. http://dx.doi.org/10.1016/j.epsr.2022.107850.

[37] Didavi ABK, Agbokpanzo RG, Agbomahena M. Comparative study of decision tree, random forest and XGBoost performance in forecasting the power output of a photovoltaic system. In: 2021 4th international conference on bioengineering for smart technologies. 2021, p. 1–5. http://dx.doi.org/10.1109/BioSMART54244.2021.9677566.

[38] Han J, Miao S, Li Y, Yang W, Yin H. Faulted-phase classification for transmission lines using gradient similarity visualization and cross-domain adaption-based convolutional neural network. Electr Power Syst Res 2021;191:106876. http://dx.doi.org/10.1016/j.epsr.2020.106876.

[39] Fan J, et al. Comparison of support vector machine and extreme gradient boosting for predicting daily global solar radiation using temperature and precipitation in humid subtropical climates: A case study in China. Energ Convers and Manag 2018;164:102–11. http://dx.doi.org/10.1016/j.enconman.2018.02.087.

[40] Memon N, Patel S, Patel D. Comparative analysis of artificial neural network and XGBoost algorithm for PolSAR image classification. 2019, p. 452–60. http://dx.doi.org/10.1007/978-3-030-34869-449,

[41] Trizoglou P, Liu X, Lin Z. Fault detection by an ensemble framework of extreme gradient boosting (XGBoost) in the operation of offshore wind turbines. Renew Energ 2021;179:945–62. http://dx.doi.org/10.1016/j.renene.2021.07.085.

[42] Raichura M, Chothani N, Patel D. Efficient CNN-XGBoost technique for classification of power transformer internal faults against various abnormal conditions. IET Gener Transmiss & Distrib 2021;15(5):972–85. http://dx.doi.org/10.1049/gtd2.12073.

[43] Wang B, Yang K, Wang D, Chen S-z, Shen H-j. The applications of XGBoost in fault diagnosis of power networks. In: 2019 IEEE innovative smart grid technologies - Asia. 2019, p. 3496–500. http://dx.doi.org/10.1109/ISGT-Asia.2019.8881495.

[44] Bentejac C, Csorgo A, Martínez-Munoz G. A comparative analysis of gradient boosting algorithms. Artif Intell Rev 2021;54:1937–67. http://dx.doi.org/10.1007/s10462-020-09896-5.

[45] Shwartz-Ziv R, Armon A. Tabular data: Deep learning is not all you need. Inf Fusion 2022;81:84–90. http://dx.doi.org/10.1016/j.inffus.2021.11.011.

[46] Blair SM, Coffele F, Booth CD, Burt GM. An open platform for rapid-prototyping protection and control schemes with IEC 61850. IEEE Trans Power Del 2013;28(2):1103–10. http://dx.doi.org/10.1109/TPWRD.2012.2231099.

[47] Salazar JJ, Garland L, Ochoa J, Pyrcz MJ. Fair train-test split in machine learning: Mitigating spatial autocorrelation for improved prediction accuracy. J Petro Sci and Eng 2022;209:109885. http://dx.doi.org/10.1016/j.petrol.2021.109885.